AUTHOR(S)
Maruyama, D., Iida, H., Koshino, K., Nakagawara, J., Morita, Y., Hashimura, N., Mori, H., Satow, T., Takahashi, J. C., Fukuda, T., Iihara, K., & Kataoka, H.

TITLE
Comparative analysis of peri-nidal cerebral blood flow and metabolism using a novel quantitative 15O-PET method in patients with arteriovenous malformations

YEAR
2024

DOI
10.1177/0271678x241270416

CITATION
Maruyama, D., Iida, H., Koshino, K., Nakagawara, J., Morita, Y., Hashimura, N., Mori, H., Satow, T., Takahashi, J. C., Fukuda, T., Iihara, K., & Kataoka, H. (2024). Comparative analysis of peri-nidal cerebral blood flow and metabolism using a novel quantitative 15O-PET method in patients with arteriovenous malformations. *Journal of Cerebral Blood Flow & Metabolism*. https://doi.org/10.1177/0271678x241270416

VERSION
Accepted Manuscript

Title: Comparative Analysis of Peri-Nidal Cerebral Blood Flow and Metabolism Using a Novel Quantitative ^{15}O-PET Method in Patients with Arteriovenous Malformations

Author Name: Daisuke Maruyama[1], Hidehiro Iida[2,3], Kazuhiro Koshino[3], Jyoji Nakagawara[1], Yoshiaki Morita[4], Naoki Hashimura[1], Hisae Mori[1], Tetsu Satow[1], Jun C Takahashi[1], Tetsuya Fukuda[4], Koji Iihara[1], Hiroharu Kataoka[1]

Affiliations:

[1]Department of Neurosurgery, National Cerebral and Cardiovascular Center, Osaka, Japan

[2]Turku PET Centre, University of Turku, Turku, Finland

[3]Department of Investigative Radiology, National Cerebral and Cardiovascular Center, Osaka, Japan

[4]Department of Radiology, National Cerebral and Cardiovascular Center, Osaka, Japan

Corresponding author: Daisuke Maruyama, M.D.

Present address: Department of Neurosurgery, Kyoto Prefectural University of Medicine

465 Kajii-cho, Kawaramachi Hirokoji, Kamigyo-ku, Kyoto 602-8566, Japan

Telephone number: +81-75-251-5541

FAX: +81-75-251-5544

E-mail: d.maru1214@gmail.com

Running headline: A novel PET method for arteriovenous malformations

Abstract

To effectively treat cerebral arteriovenous malformations (AVMs), peri-nidal flow regulation and metabolic status must be understood. In this study, we used ^{15}O-oxygen positron emission tomography (PET) post-processing analysis to investigate vascular radioactivity in the nidal region of AVMs. Single-dynamic PET imaging was performed on seven unruptured AVM patients during the sequential inhalation of $^{15}O_2$ and $C^{15}O_2$. A previously validated dual-tracer basis function method (DBFM) was employed to calculate parametric images. The results of our study were as follows. First, in remote and contralateral AVM regions, DBFM and a previous approach of dual-tracer autoradiography (DARG) showed strong positive correlations in cerebral blood flow (***CBF***), cerebral oxygen metabolism rate (***CMRO$_2$***), and oxygen extraction fraction. Second, peri-nidal ***CBF*** and ***CMRO$_2$*** correlation was lower, and overestimation occurred with DARG compared to with DBFM. Third, on comparing DBFM to quantitative ^{123}I-iodoamphetamine single-photon emission computed tomography (SPECT), ***CBF*** correlated significantly. In contrast, the correlation between DARG and quantitative ^{123}I-iodoamphetamine-SPECT was weaker in the peri-nidal regions. Fourth, analysis of time-activity curves demonstrated good reproducibility using the novel formulation in the control, peri-nidus, and core nidal regions, indicating the adequacy of this approach. Overall, the DBFM approach holds promise for assessing haemodynamic alterations in patients with AVMs.

Keywords: Arteriovenous malformation, Dual-tracer basis function method, Positron emission tomography, Single-photon emission computed tomography, Haemodynamics

Introduction

Cerebral arteriovenous malformations (AVMs) are rare vascular deformities characterised by an arteriovenous shunt from arterial feeders through a vascular nidus into cerebral veins.[1] The primary concern in managing cerebral AVMs is haemorrhage, occurring in approximately 2% of unruptured cases annually[2] and resulting in high morbidity (23–40.5%)[3,4] and mortality (12–66.7%).[5–7] Other clinical issues include epilepsy, progressive neurological symptoms, and headaches. Previous research has investigated cerebral AVM development, growth, and rupture pathophysiology, which remains unclear.[8] The core physiological characteristics include an arteriovenous shunt in the nidus and surrounding tissue, hypotension in the feeding artery, and hypertension in the draining venous system.[9] However, there is discordance among the various modalities used to investigate this pathophysiology,[9] leading to controversy and a lack of precise understanding. One representative question is whether vascular stealing through high-flow shunting exists in adjacent brain tissue.[9] An accurate understanding of haemodynamics in the intra-nidus region and oxidative metabolic status in the peri-nidus region is crucial for effective therapeutic management.

Positron emission tomography (PET) is considered the gold standard for evaluating cerebral blood flow (***CBF***), cerebral oxygen metabolism rate (***$CMRO_2$***), oxygen extraction fraction (***OEF***), and cerebral blood volume (***CBV***). However, limitations have surfaced when applying PET to patients with AVM. For example, one

common method that involves correcting for vascular radioactivity using the ***CBV*** image obtained from a ^{15}O-carbon monoxide (^{15}O-CO) inhalation scan was observed to be insufficient.[10] Additional limitations are attributed to the logistical complexity including a relatively long examination time and the need for a large technical staff to operate the cyclotron and produce radiopharmaceuticals.

Recently, a novel technique called the dual-tracer basis function method (DBFM) has emerged, allowing extremely rapid measurements to provide equally or even more accurate quantitation from a single short dynamic PET image lasting 6–8 min. This image is acquired during the sequential administration of ^{15}O-O_2 and ^{15}O-CO_2 or intravenous $H_2{}^{15}O$.[11,12] This method enables simultaneous calculation of ***CBF*** and ***$CMRO_2$*** without requiring an additional $C^{15}O$ scan. Vascular radioactivity is compensated for by incorporating vascular activity terms in the kinetic formulation. Automated radio gas production and inhalation control enable easier routine operation, thus simplifying routine ^{15}O-Gas PET examinations. Not assuming fixed arterial and venous blood volume fractions was considered advantageous, especially in areas where arterial-to-venous vascular volume fractionations were likely altered. We hypothesised that this novel approach would accurately estimate ***$CMRO_2$***, ***CBF,*** and ***OEF*** in regions where ***CBV*** is increased in patients with AVMs.

Thus, this study aimed to evaluate the effectiveness of DBFM in accurately measuring ***CBF***, ***$CMRO_2$***, and ***OEF*** in patients with AVMs. Additionally, we compared

the results obtained from this technique with those from the previously validated dual-tracer autoradiography (DARG) method, which utilises ^{15}O-CO-based ***CBV*** information by assuming fixed arterial-to-venous blood volume fractions.[13]

Material and Methods

Study design

Between March 2013 and June 2015, 20 patients with cerebral AVMs were examined using ^{15}O-PET at our institute. Among them, seven patients (5 women; mean age, 34.3 ± 13.1 years [range: 23–59 years]) with unruptured cerebral AVMs who underwent ^{15}O-PET and ^{123}I-iodeamphetamine (IMP) SPECT were enrolled in this study. The inclusion criteria comprised (1) age ≥18 years, (2) AVMs confirmed by catheter angiography, and (3) modified Rankin scale score of 0 or 1 at the time of examination. Patients with imaging evidence of previous AVM haemorrhage or prior interventional treatment attempts were excluded. The patient's baseline characteristics were obtained through medical record reviews.

The study protocol adhered to the Declaration of Helsinki and was approved by the Ethics Committee of the National Cerebral and Cardiovascular Centre (approval number: M30-013-2). The requirement for written informed consent was waived due to the study's retrospective nature.

PET scan

PET scans were conducted to quantitatively assess ***CBV***, ***CBF***, ***$CMRO_2$***, and ***OEF*** following the single-scan dual-tracer administration (SSDA) protocol, employing the previously validated DBFM[11] and DARG[13] method. Our institute employed a recently developed[12,13] automated radiosynthesis/inhalation control system that produces and inhales a series of ^{15}O-labelled gaseous radiopharmaceuticals ($C^{15}O$, $^{15}O_2$, and $C^{15}O_2$) at short intervals. These radio gases were effectively inhaled using a dedicated double-layered, double-hole facemask while monitoring end-tidal CO_2 ($EtCO_2$) and the respiratory rate throughout the PET study.[12] The PET scanner used was a Biograph mCT from Siemens Medical Solutions (Knoxville, TN, USA), which was operated in 3D mode with the outside scatter correction option disabled to enhance PET image accuracy when gaseous radioactivity surrounded the patient's face.[14] PET images were reconstructed using a standard filtered back-projection technique on the PET scanner console, incorporating corrections for scatter, attenuation, dead-time count losses, random events, and radioactivity decay. A post-reconstruction Gaussian filter with an 8-mm full width at half maximum was applied.

Following a CT scan for attenuation and scatter corrections, a 4-min scan commenced 3 min after the completion of a 3-min supply of 3,600 MBq of $C^{15}O$ to the dedicated facemask. After a 10-min wait for radioactive decay, a single dynamic scan was initiated for 480 s. Sequential inhalation of $^{15}O_2$ (2,400 MBq supply for 1 min),

followed by $C^{15}O_2$ (2,000 MBq supply for 1 min), occurred at 4.5-min intervals. The PET scan sequence comprised six intervals of 10 s, six intervals of 20 s, five intervals of 30 s, 12 intervals of 5 s, and nine intervals of 10 s, totalling 480 s of PET imaging. The net doses administered to the patients were approximately 540 MBq for $C^{15}O$, 320 MBq for $^{15}O_2$, and 520 MBq for $C^{15}O_2$, determined using a dedicated pair of radio detectors.[12] Before radio gas inhalation, radiochemical and chemical purities were confirmed to be >99% using a Rapid Gas Chromatograph (MicroGC-990, Agilent, Santa Clara, CA, USA).

During the PET scan, arterial blood was continuously drawn from the brachial artery through a catheter (0.5 mm inner diameter) using a syringe pump (Harvard Apparatus, Model 901; Holliston, MA, USA) set at a 2.0 mL/min flow rate. Blood radioactivity concentration was measured using a GSO input function monitor system (Molecular Imaging Labo, Suita, Japan). The total volume of blood withdrawn was <30 mL for each patient.

SPECT scan

The quantitative SPECT scan was conducted on all patients within 2 weeks following the PET examinations to generate quantitative regional ***CBF*** images using the IMP-ARG method,[15,16] which was suspected to be insensitive to the presence of vascular radioactivity attributed to a much higher tissue-to-blood partition coefficient or the distribution volume of 35-47 mL/mL, while IMP kinetics followed the single-tissue

compartment model fairly well.[15-18] Accurate CBF quantitation was achieved through a single ^{123}I-IMP administration, following a validated protocol outlined in previous studies.[19–24] The methodology is based on quantitative SPECT reconstruction, including well-validated corrections for photon attenuation with an accurately delineated head contour[22] and scatter and high-energy penetrating photons. The single dynamic SPECT scans, lasting 28 min, comprised seven frames of 4 min each. ^{123}I-IMP (a 167 MBq dose calibrated at noon) was infused over 1 min into the antecubital vein. A single arterial blood sample was collected to calibrate the standardised arterial input function (AIF) at 10 min post-infusion, which was the timing at which the errors caused by the individual differences in AIF effects owing to individual variations in the AIF shape from the standardised AIF were minimised.[15,16,21,25,26] The whole-blood radioactivity concentration in this sample was measured using a well counter cross-calibrated to the SPECT images, and this concentration was used to calibrate the metabolite-free AIF, which was assessed as the octanol-extracted component of the radioactivity concentrations.[25]

MRI protocol

MRI was conducted using a standard head coil on a Verio 3T system (Siemens Healthineers AG, Erlangen, Germany). Multislab three-dimensional TOF MR angiography (MRA) was used to examine the AVM structure, including feeding arteries,

nidus, draining veins, and normal cerebral arteries. The following scanning parameters were used: echo time, 3.69 ms; repetition time, 25.0 ms; field of view, 17.5 × 20.0 cm; matrix size, 384 × 261; and slice thickness, 0.6 mm.

Kinetic formulation for DARG and DBFM

Functional images for ***CBF***, ***CMRO₂***, ***OEF,*** and ***CBV*** were calculated using two in-house programmes following the DARG[13] and DBFM[11] methodologies. For both methods, the tissue radioactivity curve ($C_i\ (t)$) during the sequential inhalation of ^{15}O-O_2 and ^{15}O-CO_2 gases is expressed as follows[11,27]:

$$\boldsymbol{C_i\ (t) = (1 - V_o\ ) \cdot OEF \cdot f \cdot A_o\,(t) \otimes e^{-\frac{f}{p}\cdot t}}$$

$$\boldsymbol{+\ (1 - V_w\ ) \cdot f \cdot A_w(t) \otimes e^{-\frac{f}{p}\cdot t}}$$

$$\boldsymbol{+\ V_o\ \cdot A_o\,(t) + V_w \cdot A_w(t)},\qquad \text{Eq. (1)}$$

where $\boldsymbol{f}$ denotes the ***CBF***, $\boldsymbol{p}$ indicates the tissue-to-blood partition coefficient of water, and $\boldsymbol{V_o}$ and $\boldsymbol{V_w}$ represent the fractional blood volume for ^{15}O-O_2 and ^{15}O-H_2O, respectively. The $\otimes$ denotes the convolution integral, and $\boldsymbol{A_o(t)}$ and $\boldsymbol{A_w(t)}$ represent the AIF for ^{15}O-O_2 and ^{15}O-H_2O, respectively, where the sum of $\boldsymbol{A_o(t)}$ and $\boldsymbol{A_w(t)}$ represents the total blood radioactivity concentration, i.e., $\boldsymbol{A_{total}(t) = A_o(t) + A_w(t)}$. The first term in Eq. (1) signifies the tissue radioactivity response to ^{15}O-O_2 administration; the second term denotes the sum of the responses to metabolised ^{15}O-H_2O generated gradually from

^{15}O-O_2 as a result of body metabolism; and the third and fourth terms correspond to the vascular radioactivity contributions of ^{15}O-O_2 and ^{15}O-H_2O, respectively.

Calculation of parametric images by DARG

We first derived CBV images from a C^{15}O image to implement the DARG method. Subsequently, the contributions of arterial blood in a local region to ^{15}O-O_2 (V_o) and ^{15}O-H_2O (V_w) were calculated as follows:

$$V_o = \boldsymbol{CBV} \times \boldsymbol{(1 - OEF \times F_{vein})} \quad \text{Eq. (2a)}$$

and

$$V_w = \boldsymbol{CBV} \times \boldsymbol{(1 - F_{vein})}. \quad \text{Eq. (2b),}$$

where we assumed a fractional venous blood volume ($\boldsymbol{F_{vein}}$) of 0.835, as proposed by Mintun et al. for a three-step autoradiography technique.[28] These equations assume that the vascular activity for ^{15}O-O_2 distributes both in the arteriole with the same concentration as in the arterial blood and the venules with the non-extracted ^{15}O-O_2 concentration from the blood to the tissue, while that for ^{15}O-H_2O is mostly localised in the arteriole.

Two sets of accumulated images were used to generate functional images of ***CBF*** and ***OEF*** following the DARG method: one at the beginning of ^{15}O-O_2 inhalation for 2 min and the other at the beginning for 3 min.[13] The numerical calculation procedure closely resembled that of the three-step autoradiography of Mintun et al.[28] except that the

SSDA protocol was employed. This protocol accounts for the spillover of radioactivity administered during the first to the second scans after the inhalation of the second radioactive gas both in the arterial blood and brain tissue. It estimated the contribution of recirculating ^{15}O-H_2O following a validated physiological model.[11]

Calculation of parametric images by DBFM

In the DBFM, PET images from the scan period (0–480 s) were employed to calculate four parametric images (***CBF***, ***OEF***, $\boldsymbol{V_o}$, and $\boldsymbol{V_w}$) using a nonlinear least squares fitting (NLLSF) optimisation with the grid search technique.[11] The convolution terms ($A_o\ (t) \otimes e^{-\frac{f}{p} \cdot t}$ and $A_w(t) \otimes e^{-\frac{f}{p} \cdot t}$) were tabulated as two sets of basis functions in terms of ***CBF*** (***f***) to reduce the computation time. Using a typical Windows PC, the actual calculation time to generate all four parametric images was <10 s.

$\boldsymbol{CMRO_2}$ images were then calculated as the product of ***CBF*** (***f***), ***OEF,*** and the oxygen content in arterial blood ($\boldsymbol{[O_2]_a}$] for both the DARG method and DBFM as follows[28]:

$$\boldsymbol{CMRO_2} = \boldsymbol{[O_2]_a} \times \boldsymbol{CBF} \times \boldsymbol{OEF}. \qquad \text{Eq. (3)}$$

Here, $\boldsymbol{[O_2]_a}$ is the product of the oxygen volume confined per gram of haemoglobin (1.39 [mL/g]), the haemoglobin concentration in the blood [g/mL], and the fractional saturation of oxygen in arterial blood (e.g., 98%).

Estimation of metabolised ^{15}O-H_2O and ^{15}O-O_2 input functions

The metabolised ^{15}O-H_2O curve ($\boldsymbol{A_w(t)}$) was estimated from the total blood AIF $A_{total}(t)$[29] as:

$$\boldsymbol{A_w(t)} = \boldsymbol{k_w} \times \boldsymbol{A_{total}(t)} \otimes e^{-\boldsymbol{k_w} \cdot \boldsymbol{t}}, \quad \text{Eq. (4a)}$$

where $\boldsymbol{k_w}$ [min^{-1}] represents the production rate of the metabolised ^{15}O-H_2O in arterial blood after ^{15}O-O_2 inhalation. The ^{15}O-O_2 AIF, $\boldsymbol{A_o(t)}$, was obtained until the initiation of ^{15}O-CO_2 inhalation as follows:

$$\boldsymbol{A_o(t)} = \boldsymbol{A_{total}(t)} - \boldsymbol{A_w(t)}. \quad \text{Eq. (4b)}$$

The $\boldsymbol{A_o(t)}$ curve was extrapolated after ^{15}O-CO_2 administration, such that $\boldsymbol{A_w(t)}$ was calculated as follows:

$$\boldsymbol{A_w(t)} = \boldsymbol{A_{total}(t)} - \boldsymbol{A_o(t)} \quad \text{Eq. (4c)}$$

Image analysis

All PET, SPECT, and MRA images were transferred to an independent PC workstation for further analysis. MRA images were registered to the PET-CBF image calculated by the DBFM using Multimodality Image Registration Software (PVElab[30]). SPECT images were also registered to the DBFM-based PET-CBF image, ensuring that PET, MRA, and SPECT images were aligned at the same coordinates. Visual confirmation was conducted to ensure agreement between the registered images,

verifying the alignment of brain contours across PET, MRA, and SPECT images, including the cerebellum, Sylvian fissure, and ventricular regions.

Regions of interest (ROIs) were defined according to the following six criteria on MRA images:

(a) ipsilateral peri-nidus region (ROI-pi)

(b) ipsilateral remote region (ROI-ri)

(c) contralateral peri-nidus region (ROI-pc)

(d) contralateral remote region (ROI-rc)

(e) ipsilateral intra-nidus region (ROI-n)

(f) ipsilateral transitional border of the nidus region (ROI-t)

All ROIs (20-mm diameter) were selected using QView software (Version 3.0.3) developed by the QSPECT project (National Cerebral and Cardiovascular Center Research Institute, Osaka, Japan).[19] These ROIs were superimposed on the ***CBF***, ***CMRO$_2$***, and ***OEF*** images obtained from PET- and SPECT-based ***CBF*** images (**Figure 1**).

Remote ROIs on the ipsilateral hemisphere (ROI-ri) comprised 10 regions, including the cerebellum, thalamus, front polar, anterior middle cerebral, posterior middle cerebral, posterior, and corona radiata, avoiding any part within 20 mm of the nidus border (**Figure 1A**). Ipsilateral peri-nidus ROIs (ROI-pi) were positioned at 10 locations surrounding the nidus on the ipsilateral hemisphere, avoiding prominent vessels or high

CBV regions (**Figure 1B)**. The ROIs mirroring the remote and peri-nidus regions on the contralateral hemisphere were designated as ROI-rc and ROI-pc, respectively (**Figure 1**).

Statistical analysis

Measured parametric values are presented as the mean ± 1 standard deviation (SD) for each ROI. Pearson's correlation analysis was used to evaluate the ***CBF***, ***$CMRO_2$***, and ***OEF*** relationships between DARG and DBFM, the ***CBF*** between DBFM and ^{123}I-IMP SPECT, and the ***CBF*** between DARG and ^{123}I-IMP SPECT. Statistical significance was determined as $p < 0.05$. Analyses were conducted using the JMP software package (version 17.1.0; SAS Institute Inc., Cary, NC, USA).

Results

Table 1 summarises the baseline characteristics of the study cohort. All AVMs were unruptured and located supratentorially, with five in the lobar region and two in the basal ganglia. Clinical manifestations included progressive neurological deficits in two patients and epilepsy in two others. In the remaining three patients, the AVMs were incidentally diagnosed. Seizures in two patients with a history of epilepsy were well controlled during PET and SPECT studies using anticonvulsant medications. All patients underwent cerebral angiography before the PET and SPECT studies. The maximum diameter of the AVMs' nidus ranged from 30 to 70 mm. According to the Spetzler–Martin

grade,[31] there were four Grade III, one Grade V, and two Grade IV AVMs. No hyperintense lesions indicating brain oedema on FLAIR or hypointense lesions indicating microbleeds on T2* were observed on MRI. A total of 52 regions were analysed for ROI-ri and ROI-rc and 67 regions for ROI-pi and ROI-pc. Quantitative values of ***CBV***, ***$CMRO_2$***, and ***OEF*** from DARG and DBFM and ***CBF*** values from DARG, DBFM, and ^{123}I-IMP SPECT are listed in **Supplementary Tables 1 and 2**.

Representative case images

Figure 2 shows a left temporal AVM example (Case 2). The nidus and associated venous sinuses were visualised as high blood volume in the ***CBV*** image obtained through ^{15}O-CO inhalation PET. The DARG method was used to calculate the ***CBF*** and ***$CMRO_2$*** images, indicating high values in regions with high ***CBV*** **(Figure 2B)**. Notably, ***CBF*** and ***$CMRO_2$*** were elevated in the anterior peri-nidal region when calculated using the DARG method (arrows). Conversely, the DBFM **(Figure 2A)** did not show apparent increases in ***CBF*** or ***$CMRO_2$*** in regions with increased ***CBV***. The $\boldsymbol{V_o}$ and $\boldsymbol{V_w}$ images showed high values in regions with increased ***CBV***. There was an apparent increase in $\boldsymbol{V_o}$ compared to $\boldsymbol{V_w}$ around the global brain and sinus vessels, mirroring the ***CBV*** distribution. The visibility of the sinus vessels in the $\boldsymbol{V_w}$, shown by arrowheads **(Figure 2A),** is unique because it is not observed in healthy individuals or most patients with cerebral vascular diseases as typically shown in the previous work.[11] As shown in

Figure 2C, the ***CBF*** image obtained using quantitative ^{123}I-IMP SPECT did not increase in this region, which aligns with the DBFM-based ***CBF*** results. The nidus defined using MRA correlated with the high accumulation of ***CBF*** and ***CMRO$_2$*** obtained using DARG and ***CBV***. Digital subtraction angiography revealed a high-flow arteriovenous shunt of the right temporal lobe nidus draining into the superior sagittal and right transverse sinuses.

Time-activity curve analysis

Figure 3 shows a representative result from the NLLSF analysis for the simultaneous fitting of ***CBF***, ***OEF***, $\boldsymbol{V_o}$, and $\boldsymbol{V_w}$ to time-activity curves (tTACs) obtained from individual PET scans during the sequential inhalation of ^{15}O-O_2 and ^{15}O-CO_2. It should be noted that all AIFs and tTACs were not corrected for the radioactivity decay of ^{15}O. This analysis was performed on the slice delineated by the red line in **Figure 2**. The AIFs for ^{15}O-O_2 ($\boldsymbol{A_o(t)}$), ^{15}O-H_2O ($\boldsymbol{A_w(t)}$), and total blood ($\boldsymbol{A_{total}(t)}$) from this scan are shown in **Figure 3A**. $\boldsymbol{A_o(t)}$ peaked in the early phase, followed by a monotonic decrease until the end of the scan. $\boldsymbol{A_w(t)}$ gradually increased after initiating ^{15}O-O_2 inhalation, reaching the same level as $\boldsymbol{A_o(t)}$ at approximately 200 s. Subsequently, $\boldsymbol{A_w(t)}$ increased after inhaling ^{15}O-CO_2, peaked at 360 s, and then decreased. **Figure 3B** shows the regional tTAC in the remote region of the contralateral hemisphere of the nidus lesion (ROI-pc), demonstrating that

the measured tTAC was effectively replicated by the summation of the four components described in Eq. (1). Notably, the blood radioactivity component, $\boldsymbol{V_o \cdot A_o(t)}$, contributed to reproducing the early phase of the tTAC for the ^{15}O-O_2 inhalation. On the other hand, the contribution of $\boldsymbol{V_w \cdot A_w(t)}$ was not apparent for the ^{15}O-CO_2 inhalation tTAC (well reproduced by Ci(t) using Eq. (2) even without the second term of Eq. (2) ($\boldsymbol{V_w \cdot A_w(t)}$)) despite significant presence in the component. This is because vascular activity for ^{15}O-H_2O is mostly localised in the arteriole in the control region that has been assumed to have a volume fraction of ($1-F_{vein} \fallingdotseq 0.165$ ml/ml), where it has the same concentration in the venule as that in the tissue, making the vascular radioactivity negligible. **Figures 3C–E** show the tTACs for the ipsilateral ROIs, namely, the peri-nidus (**C**), transitional border of the nidus (**D**), and intra-core of the nidus (**E**). The measured data were well reproduced by the sum of the simulated tTACs defined by Eq. (1), which comprises four components: tTAC as a response to the ^{15}O-O_2 and ^{15}O-CO_2 administration and contributions of $\boldsymbol{V_w \cdot A_w(t)}$ and $\boldsymbol{V_o \cdot A_o(t)}$. It can be seen that all four components are significant in reproducing the measured tTACs reasonably well in all three regions. Notably, while the tTACs for the vascular components (red lines) are proportional to the $\boldsymbol{A_o(t)}$ and $\boldsymbol{A_w(t)}$ curves, as indicated in the third and fourth terms of Eq. (1), the relative heights of the peaks of the red curves varied between ROIs. In **B** and **C**, the first peak ($\boldsymbol{V_o \cdot A_o(t)}$) is bigger,

but they are almost equal in **D**, with the second peak ($V_w \cdot A_w(t)$) becoming bigger in **E**.

An additional NLLSF analysis conducted to evaluate the effects of the inadequately adjusted time delay in the AIF on the errors in the calculated parametric values demonstrated that the artificially added time shift of -3/+3 s in the AIF generated differences in the calculated ***CBF***, ***$CMRO_2$***, and ***OEF*** values by +2.3%/-2.6%, +0.9%/0.0%, and -1.4%/+2.7% of errors, respectively. The changes in V_o and V_w were larger at -14.6%/+7.6% and -40.1%/+66.1%, respectively.

There were no significant differences in the ***CBF***, ***$CMRO_2$***, and ***OEF*** values between the ROI-based and pixel-by-pixel-based calculations, using the same fitting program. However, there were variations in the differences, e.g., variations for ***CBF*** were approximately ±0.5%, ±2.6%, and ±6.4% in (a) the remote and peri-nidus, (b) transitional border, and (c) intra-nidus regions, respectively. Similarly, variations for ***$CMRO_2$*** were (a) ±0.6%, (b) 1.9%, and (c) 20.4% and those for ***OEF*** were (a) ±0.6%, (b) 3.8%, and (c) 15%, respectively. Considerably larger variations in the differences were apparent between the ROI-based and pixel-by-pixel-based calculations in areas where blood volume was larger, largely attributed to the increased variations in the pixel-by-pixel calculations.

Comparison of regional values between DBFM and DARG

Figure 4 shows the relationships between the regional ***CBF***, ***CMRO$_2$***, and ***OEF*** values of DBFM and DARG in the four ROI groups. On the contralateral side of the AVMs, we observed a high positive correlation between ***CBF*** and ***CMRO$_2$*** values using both DBFM and DARG for both ROI-rc (***CBF***: r = 0.98, $p < 0.001$; ***CMRO$_2$***: r = 0.91, $p < 0.001$) and ROI-pc (***CBF***: r = 0.98, $p < 0.001$; ***CMRO$_2$***: r = 0.92, $p < 0.001$). This positive correlation was also observed in ROI-ri on the ipsilateral side of the nidus (***CBF***: r = 0.99, $p < 0.001$; ***CMRO$_2$***: r = 0.91, $p < 0.001$). However, the correlation coefficient was lower in the ipsilateral peri-nidus regions (ROI-pi) (***CBF***, r = 0.79, $p < 0.001$; ***CMRO$_2$***, r = 0.60, $p < 0.001$). In ROI-pi, the quantitative values of ***CBF*** and ***CMRO$_2$*** tended to be overestimated when using DARG compared to DBFM. For ***OEF*** values, the same but less remarkable tendency was observed.

Comparison of regional CBF values between PET and SPECT

Figure 5 shows the correlations and Bland–Altman plots for quantitative ***CBF*** values between DBFM PET and ^{123}I-IMP SPECT, as well as between DARG PET and ^{123}I-IMP SPECT. DBFM-PET revealed significant positive correlations in ***CBF*** in both the contralateral ROI-pc (r = 0.74, p < 0.001) and ipsilateral ROI-pi (r = 0.60, p < 0.001) (**Figure 5A upper plots**). The Bland–Altman plots revealed that the difference between the two ***CBF*** values increased when the mean CBF was increased (ROI-pc: r = 0.72, p < 0.001, y = 0.71x – 17.39; ROI-pi: r = 0.69, p < 0.001, y = 0.83x – 19.62) (**Figure 5A**

lower plots). In DARG PET, significant positive correlations were also seen in ***CBF*** between DARG and ^{123}I-IMP SPECT both in the ROI-pi and ROI-pc regions. However, the correlation coefficient was smaller in ROI-pi ($r = 0.39$, $p = 0.001$) than in ROI-pc ($r = 0.75$, $p < 0.001$) (**Figure 5B upper plots**). The Bland–Altman plots showed a significant increase in the difference in ***CBF*** according to the mean ***CBF*** increase between DARG PET and ^{123}I-IMP SPECT in both ROI-pc ($r = 0.63$, $p < 0.001$, $y = 0.57x – 14.05$) and ROI-pi ($r = 0.67$, $p < 0.001$, $y = 0.98x – 21.2$) (**Figure 5B lower plots**). Solid and broken lines on each Bland–Altman plot show the mean difference and its respective 1.96 standard deviations (SD); larger deviations were seen in ROI-pi.

Figure 6 shows the correlations of ***CBF*** values between DBFM PET and DARG PET (**Figure 6A**), DARG PET and ^{123}I-IMP SPECT (**Figure 6B**), and DBFM PET and ^{123}I-IMP SPECT (**Figure 6C**) for ROIs including ROI-n, ROI-pi, and ROI-t. A large dissociation occurred between DBFM and DARG resulting in no significant correlation ($r = 0.02$, $p = 0.82$, $y = 0.0075x + 34.5$) and DARG and ^{123}I-IMP SPECT ($r = -0.20$, $p = 0.07$, $y = -1.34x + 93.17$), whereas the correlation between DBFM and ^{123}I-IMP SPECT still maintained significance ($r = 0.60$, $p < 0.001$, $y = 1.21x + 0.91$). The correlation coefficient between DBFM PET and ^{123}I-IMP SPECT was unchanged compared to the results shown in **Figure 5A** even though the added ROIs, ROI-n and ROI-t, contained a large volume of blood.

Discussion

This study demonstrated that DBFM, a novel technique, generated parametric images of ***CBF***, ***CMRO$_2$***, and ***OEF*** with no apparent influence of elevated ***CBV*** in the nidus region. The DARG method calculated vascular radioactivity using the ***CBV*** image by assuming a fixed arterial-to-venous volume fraction, resulting in high ***CBF*** and ***CMRO$_2$*** values in the nidus region (**Figure 2**). Both methods provided identical images outside the nidus core, with similar ***OEF*** values in the remote regions. The agreement between DBFM and DARG includes statistical noise. The TAC analysis shown in **Figure 3** demonstrates that the observed tissue TACs were well reproduced by adding the vascular radioactivity contributions for both ^{15}O-O_2 and ^{15}O-H_2O inhalation periods, as defined in Eq. (1), for the remote, peri-nidus, transitional, and intra-nidus regions. The fairly good agreement in most cerebral tissue, except for the nidus and peri-nidal regions, was unsurprising. This is consistent with the validation of DARG and DBFM, yielding ***OEF*** values that agree well with the ***OEF*** assessed by the arterial-venous difference in cynomolgus monkeys over a broad physiological range.

The important finding in this study was that the blood volume-equivalent images (***V$_o$*** for ^{15}O-O_2 and ***V$_w$*** for ^{15}O-H_2O) compensated well for vascular radioactivity in the parametric image calculation of ***CBF***, ***CMRO$_2$***, and ***OEF***. The ***Vo*** represents the volume of blood containing ^{15}O-O_2-labelled oxy-haemoglobin, which includes the volume in the arteriole compartment and the volume of non-extracted ^{15}O-O_2 from the

blood to the tissue, thus remaining in the venule compartment. The ***Vw*** represents the volume of the arterial blood containing ^{15}O-H_2O, which means that the blood radioactivity is present in the arteriole region, which is negligibly small in the venule compartment in a healthy brain but can be increased if shunt vessels exist. Therefore, $\boldsymbol{V_w}$ should correspond to the volume of arterial blood in the shunt vessels in the nidus and peri-nidus lesions, if this is observed as significant. It should also be noted that both $\boldsymbol{V_o}$ for ^{15}O-O_2 and $\boldsymbol{V_w}$ for ^{15}O-H_2O compensate for the errors attributed to the possible delay adjustment of the AIF relative to the tTACs because of results from the simulation analysis in which the AIF was artificially shifted to assess the error propagation to the parametric values of ***CBF*** and $\boldsymbol{CMRO_2}$. In cases in which the delay adjustment was not accurate, errors were introduced in both $\boldsymbol{V_o}$ and $\boldsymbol{V_w}$, providing only relative information. Careful adjustment procedures are needed for delay assessment if one intends to use the $\boldsymbol{V_o}$ and $\boldsymbol{V_w}$ information to characterise the pathophysiological status of the arteriovenous shunt, etc.

This study also demonstrated the following. First, strong positive correlations in ***CBF***, $\boldsymbol{CMRO_2}$, and ***OEF*** between DBFM and DARG were observed in regions on the entire contralateral side and in the remote areas on the ipsilateral side of the AVM, placed at least 20 mm away from the nidus lesion (**Figure 4**). Second, the dissociation between these two methods was observed in part of the data in the peri-nidus regions, where ***CBF*** and $\boldsymbol{CMRO_2}$ were higher with DARG than with DBFM. Third, significant correlations

were observed in ***CBF*** for both the ipsilateral peri-nidus and contralateral mirror of peri-nidal lesions between ^{123}I-IMP SPECT and DBFM PET. The correlation was stronger between ^{123}I-IMP SPECT and DBFM than between ^{123}I-IMP SPECT and DARG. Fourth, TAC analysis revealed an increased influence of radioactivity on blood vessels in the peri-nidal regions on the ipsilateral side than in remote regions on the contralateral side.

Comparison of regional values between DBFM and DARG

This study shows that the parametric images of ***CBF***, ***CMRO$_2$***, and ***OEF*** exhibit very close quality and contrast between DBFM and DARG, including the different effects of statistical noise. The DBFM eliminates high ***CBV***-associated overestimations. However, the two methods vary in the effects of TAC delay. This study assumed a standard delay parameter across the cerebral and cerebellar regions relative to the AIF. However, region-dependent errors were identified within the brain and cerebellar regions. It is known that ^{15}O-water reaches the cerebellum in a healthy population in 4–5 s compared to most cerebral tissue because the cerebellum receives arterial blood from the vertebral artery, while most cerebral tissue receives blood from the internal carotid artery.[32,33] This results in approximately 5% underestimation in DBFM and 5% overestimation in DARG in both ***CBF*** and ***CMRO$_2$*** in the cerebellar region.[11] Consequently, an approximately 10% difference can be seen in the cerebellar region.

Comparison of CBF between ^{15}O-PET methods and ^{123}I-IMP SPECT

The kinetics of ^{123}I-IMP are known to follow the single-tissue compartment model well; this is the same with ^{15}O-H_2O. It is also known that ^{123}I-IMP has a considerably larger distribution volume ($\boldsymbol{V}_d$ = 35–47 mL/mL)[16,17,34] than that of ^{15}O-H_2O ($\boldsymbol{V}_d$ = 0.8–1.0 mL/mL).[33] Additionally, ^{123}I-IMP stays in the blood circulation remaining unmetabolised at 0.70±0.09 at 40 min and 0.50±0.039 at 180 min after an i.v. injection of ^{123}I-IMP in humans. The larger $\boldsymbol{V}_d$ causes the peak of the tissue activity concentration relative to that of AIF to be approximately 40 times greater in ^{123}I-IMP SPECT than in ^{15}O-H_2O PET. It should also be mentioned that the early appearance of peak AIF could easily be avoided during the SPECT imaging period, whereas in ^{15}O-H_2O PET, the period in which the AIF still has a high radioactivity concentration should have been included. The ability of ^{123}I-IMP SPECT to provide quantitative ***CBF*** images has been fairly well validated in several ways. Therefore, the use of ^{123}I-IMP SPECT is adequate to qualify the adequacy of the DBFM to eliminate the effects of blood radioactivity in patients with AVMs. As shown in **Figures 5 and 6**, the DARG technique, which utilised the traditional assumption of fixed $\boldsymbol{F_{vein}}$, failed to yield a good agreement with the ^{123}I-IMP SPECT images in the nidus core, transitional border, and peri-nidus lesions. On the other hand, DBFM yielded a reasonable agreement with the ^{123}I-IMP SPECT images. Notably, ^{123}I-IMP SPECT has considerably worse spatial resolution, which leads to systematic underestimation in high-***CBF*** regions and overestimation in low-***CBF*** regions when

compared with PET. This explains the ***CBF***-dependent difference observed in the Bland-Altman plot analyses between PET measurements with DBFM and DARG and ^{123}I-IMP SPECT measurements as shown in **Figure 5**. However, extensive efforts to improve the ^{123}I-IMP SPECT technique[19,21,25,26], involving quantitative reconstruction, standardised SPECT scan procedures, and fairly well-developed post-processing image analysis programs, have enabled the quantitative assessment of ***CBF*** values at rest and after pharmacological challenges with acetazolamide, providing fairly good reproducibility in the same subjects and even among institutions or different SPECT systems. Quantitative ^{123}I-IMP SPECT can contribute to certain areas in clinical settings as demonstrated earlier.[19]

Controversies in the pathophysiology of AVMs

There has been controversy concerning the steal phenomenon or haemodynamic impairment in peri-nidal brain tissue.[35] One year before the first successful resection of cerebral AVMs in 1889, Gowers et al. described a condition called ‘congestive apoplexy’ as the most severe complication of cerebral congestion.[36] Spetzler et al. described this phenomenon after AVM resection as a normal perfusion pressure breakthrough[37] induced by a rapid overload of blood flow in the associated arterioles with a loss of constrictive function. Tyler et al. reported in their PET study that although ***CBF*** was maintained, a type of steal phenomenon existed, as evidenced by a tendency towards

a rising ***OEF*** in the cerebral cortex around the AVMs.[38] Other studies have reported decreased ***CBF*** in surrounding areas, leading to a propensity for seizures and cognitive impairment in SPECT studies,[39] or a significant increase up to normal levels after resection, resulting in clinical improvement of neurological deficits in the Xe-CT study.[40] Ten of the 13 patients with cerebral AVMs exhibited low baseline ***CBF*** that failed to increase with acetazolamide administration in perfusion CT methods, indicating an impaired vascular reserve.[41] However, some studies reported no cerebral hypoperfusion caused by arterial hypotension, attributing the low ***CBF*** near the nidus to the heterogeneity of the normal cortex,[42] mass-reflected factors, or neurogenic factors such as neuronal deafferentation and diaschisis[43,44] in microspectrophotometry,[42] SPECT,[43] and transcranial Doppler ultrasonography[44] studies. Young et al. argued in an intra-arterial microcatheter study that autoregulation was preserved by a shift of the autoregulation curve to the left in the chronically hypotensive peri-nidal cortex.[45] Al-Rodhan proposed their theory of occlusive hyperaemia, stating that postoperative haemorrhage or oedema is due to venous outflow obstruction of the adjacent parenchyma with resultant passive hyperaemia or stagnant arterial flow in former AVM feeders, worsening hypoperfusion of any parenchyma with which the feeders may have been associated.[46] The main problem with these controversies is the lack of a standardised and validated method to observe cerebral haemodynamics.[9] PET scans are institutionally

limited; however, our novel PET method could provide a highly reliable standard for intracranial shunt disease by evaluating ***CBF***, ***CBV***, ***$CMRO_2$***, and ***OEF***.

Iwama et al. reported cerebral haemodynamics and metabolism in patients with AVMs using PET scanning with the steady-state method.[47] In their analysis, the ***CBF*** values were significantly lower and ***OEF*** and ***CBV*** values were significantly higher in the peri-nidal ROI than in the contralateral ROI in cases with high-flow AVMs, large AVMs, or progressive neurological deficits. The peri-nidal ROI was set in regions close to the nidus and fed by the main trunk of the feeding artery. Although the exact distance between the margin of the nidus and the ROI is unclear, they were not within a few millimetres of each other in their figures. Other haemodynamic studies on AVMs have indicated impaired cerebrovascular reserve (CVR) in patients with seizures using a BOLD MRI study.[48] They suggested that impaired peri-nidal CVR is strongly associated with epileptogenic seizure presentation. Utilising the high spatial resolution of MRI, they evaluated CVR at 2-mm intervals within 10 mm of the nidus and found higher impairment as close as possible. Their study indicated the importance of exact haemodynamic evaluation, including metabolism, in regions close to the nidus. This finding highlights the significance of our study.

Peri-nidal pathophysiologic findings of this study

Our TAC analysis revealed the fundamental pathophysiology in peri-nidal regions that contain more radioactive blood vessels than in ipsilateral and contralateral remote regions. This finding is based on the existence of small, fragile, looped vessels commonly found in the deep white matter around the nidus[49] or a markedly dilated capillary network. This network not only connects AVM components but also forms connections with the normal capillary network and could explain the recurrence or reappearance of cerebral AVMs, often referred to as the 'peri-nidal dilated capillary network'.[50] Regardless of the anatomical pathology, this TAC analysis indicates the superiority of DBFM over the former techniques, including DARG and 3-step autoradiography, in evaluating peri-nidal regions. Furthermore, this finding may explain and support previously reported elevated ***CBV*** values in peri-nidal regions.

Limitations and future studies

This study had a few limitations. First, the sample size was small, as this primitive sensitivity analysis aimed to evaluate a novel methodology. Patients were selected only if they had unruptured AVMs or no brain oedema. Further studies are needed to investigate haemodynamic correlations between ruptured and unruptured AVMs, large and small AVMs, AVMs with and without oedema, and symptomatic and asymptomatic AVMs. Second, the spatial resolutions of MRI, ^{15}O-PET, and ^{123}I-IMP SPECT were approximately 0.5 mm, 7 mm, and 15 mm, respectively. Despite a filtering

process for the PET images, this could cause bias when comparing the ROI parameters in different modality images. The MRA images, defined as the ROI, had the highest spatial resolution. Although we intended to minimise possible spillovers from the nidus region, there was no evidence to prove the absence of spillover effects. Third, the ROI setting for each patient was arbitrary, especially in the peri-nidal ROI. The peri-nidal ROI was set as close as possible to the nidus to elucidate the significance of this novel PET method. Further validation of this ROI setting is necessary. Fourth, TAC analysis described in this study, as well as the quantitative parametric images of $\boldsymbol{V}_{\mathrm{o}}$ and $\boldsymbol{V}_{\mathrm{w}}$, has a potential application in visually assessing the enlarged volume of blood vessel compartments and could be a possible way to evaluate the pathophysiological conditions in certain regions associated with symptoms or treatments. It is worth noting that we did not observe systematic differences in the quantitative parametric values between the ROI-based fitting and pixel-by-pixel calculation-based approaches. We interpret this as being attributed to the use of the grid-search algorithm employed in NLLSF in this study, possibly because global optimisation could have been successfully achieved. However, statistical fluctuations were enhanced in areas of increased $\boldsymbol{V}_{\mathrm{o}}$ and $\boldsymbol{V}_{\mathrm{w}}$. This could be an issue that should be further investigated to improve the technique. Fifth, tissue heterogeneity within the selected ROIs is known to cause systematic errors, e.g., quantitation of ***CBF*** and $\boldsymbol{CMRO_2}$ in a healthy brain can be underestimated by a maximum of approximately 20% due to the mixture of grey and white matter tissues.[51] The

magnitude of errors was shown to be further enhanced in tumour tissues.[52] Further studies should be conducted to understand the effects of the heterogeneous tissue structure in pathophysiological conditions in patients with AVM.

In conclusion, the findings in this article suggest the validity of DBFM as a novel strategy to evaluate the peri-nidal regions more accurately in patients with AVMs using ***CBF***, ***$CMRO_2$***, and ***OEF***, offering potential advancements for exploring therapeutic approaches more comprehensively.

Acknowledgements

The authors thank the staff of National Cerebral and Cardiovascular Center for their technical assistance with positron emission tomography, SPECT, and magnetic resonance imaging.

Author Contribution Statement

Daisuke Maruyama:

Project management, project initiation, patient selection, study design, data analysis, and writing of the original draft.

Hidehiro Iida:

Study design from the methodological side, kinetic model analysis design, post-processing data analysis software, data acquisition protocol for ^{15}O-oxygen PET, and writing and editing of the draft.

Kazuhiro Koshino:

Methodology for image analysis, data curation, and editing of the draft.

Jyoji Nakagawara:

Methodology for ^{123}I-IMP SPECT image analysis and editing of the draft.

Yoshiaki Morita:

Methodology and management of the MRI and editing of the draft.

Naoki Hashimura:

Data collection, curation, and editing of the draft.

Hisae Mori:

Resource for patient recruitment, conceptualisation, and editing of the draft.

Tetsu Satow:

Resources for patient recruitment, supervision of cerebral angiography, conceptualisation, and editing of the draft.

Jun C Takahashi:

Resources for patient recruitment and investigation, methodology and supervision for imaging analysis, and editing of the draft.

Tetsuya Fukuda:

Resource for imaging investigation and editing of the draft.

Koji Iihara:

Resource for patient recruitment, investigation, conceptualisation, supervision, and editing of the draft.

Hiroharu Kataoka:

Resources for patient recruitment and investigation, conceptualisation, supervision, project administration, and editing of the draft.

Funding Acknowledgements:

This work was supported by JSPS KAKENHI Grant-in-Aid for Research Activity Start-up (25893304) and Fostering Joint International Research (B) (21KK0183), and Japan Cardiovascular Research Foundation,

Disclosure of Conflicting Interest:

There is no conflict of interest to disclose for this study.

Research Ethics and Patient Consent:

The ethics committee of the National Cerebral and Cardiovascular Centre (approval number: M30-013-2)

Sentence Regarding Supplementary Information on the JCBFM Website, if any:

Supplementary material for this paper can be found at http://jcbfm.sagepub.com/content/by/supplemental-data

Availability of Data and Materials:

Not possible to share the images because of the privacy policy at the institute

Sharing Materials:

None

References

1. Solomon RA and Connolly ES, Jr. Arteriovenous brain malformations. *N Engl J Med* 2017; 377: 498. DOI: 10.1056/NEJMc1707399.

2. Mohr JP, Parides MK, Stapf C, et al. Medical management with or without interventional therapy for unruptured brain arteriovenous malformations (ARUBA): a multicentre, non-blinded, randomised trial. *Lancet* 2014; 383: 614–621. DOI: 10.1016/S0140-6736(13)62302-8.

3. Fukuda K, Majumdar M, Masoud H, et al. Multicenter assessment of morbidity associated with cerebral arteriovenous malformation haemorrhages. *J Neurointerv Surg* 2017; 9: 664–668. DOI: 10.1136/neurintsurg-2016-012485.

4. Choi JH, Mast H, Sciacca RR, et al. Clinical outcome after first and recurrent haemorrhage in patients with untreated brain arteriovenous malformation. *Stroke* 2006; 37: 1243–1247. DOI: 10.1161/01.STR.0000217970.18319.7d.

5. Fults D and Kelly DL, Jr. Natural history of arteriovenous brain malformations: a clinical study. *Neurosurgery* 1984; 15: 658–662. DOI: 10.1227/00006123-198411000-00003.

6. Brown RD, Jr., Wiebers DO, Forbes G, et al. The natural history of unruptured intracranial arteriovenous malformations. *J Neurosurg* 1988; 68: 352–357. DOI: 10.3171/jns.1988.68.3.0352.

7. van Beijnum J, Lovelock CE, Cordonnier C, et al. Outcome after spontaneous and arteriovenous malformation-related intracerebral haemorrhage: population-based studies. *Brain* 2009; 132: 537–543. DOI: 10.1093/brain/awn318.

8. Rodemerk J, Oppong MD, Junker A, et al. Ischemia-induced inflammation in arteriovenous malformations. *Neurosurg Focus* 2022; 53: E3. DOI: 10.3171/2022.4.Focus2210.

9. Moftakhar P, Hauptman JS, Malkasian D, et al. Cerebral arteriovenous malformations. Part 2: physiology. *Neurosurg Focus* 2009; 26: E11. DOI: 10.3171/2009.2.FOCUS09317.

10. Okazawa H, Yonekura Y, Sadato N, et al. Delayed data acquisition for optimal PET activation studies with oxygen-15-water in cerebral arteriovenous malformation. *J Nucl Med* 1995; 36: 2149–2153.

11. Kudomi N, Hirano Y, Koshino K, et al. Rapid quantitative CBF and CMRO(2) measurements from a single PET scan with sequential administration of dual (15)O-labeled tracers. *J Cereb Blood Flow Metab* 2013; 33: 440–448. DOI: 10.1038/jcbfm.2012.188.

12. Iguchi S, Moriguchi T, Yamazaki M, et al. System evaluation of automated production and inhalation of (15)O-labeled gaseous radiopharmaceuticals for the rapid (15)O-oxygen PET examinations. *EJNMMI Phys* 2018; 5: 37. DOI: 10.1186/s40658-018-0236-5.

13. Kudomi N, Hayashi T, Teramoto N, et al. Rapid quantitative measurement of CMRO(2) and CBF by dual administration of (15)O-labeled oxygen and water during a single PET scan- a validation study and error analysis in anaesthetised monkeys. *J Cereb Blood Flow Metab* 2005; 25: 1209–1224. DOI: 10.1038/sj.jcbfm.9600118.

14. Hori Y, Hirano Y, Koshino K, et al. Validity of using a 3-dimensional PET scanner during inhalation of 15O-labeled oxygen for quantitative assessment of the regional metabolic rate of oxygen in man. *Phys Med Biol* 2014; 59: 5593–5609. DOI: 10.1088/0031-9155/59/18/5593.

15. Iida H, Itoh H, Nakazawa M, et al. Quantitative mapping of regional cerebral blood flow using iodine-123-IMP and SPECT. *J Nucl Med* 1994; 35: 2019–2030.

16. Iida H, Akutsu T, Endo K, et al. A multicenter validation of regional cerebral blood flow quantitation using [123I]iodoamphetamine and single photon emission computed tomography. *J Cereb Blood Flow Metab* 1996; 16: 781–793. DOI: 10.1097/00004647-199609000-00003.

17. Iida H, Itoh H, Bloomfield PM, et al. A method to quantitate cerebral blood flow using a rotating gamma camera and iodine-123 iodoamphetamine with one blood sampling. *Eur J Nucl Med* 1994; 21: 1072–1084. DOI: 10.1007/BF00181062.

18. Yokoi T, Iida H, Itoh H, et al. A new graphic plot analysis for cerebral blood flow and partition coefficient with iodine-123-iodoamphetamine and dynamic SPECT validation studies using oxygen-15-water and PET. *J Nucl Med* 1993; 34: 498–505.

19. Iida H, Nakagawara J, Hayashida K, et al. Multicenter evaluation of a standardised protocol for rest and acetazolamide cerebral blood flow assessment using a quantitative SPECT reconstruction program and split-dose ^{123}I-iodoamphetamine. *J Nucl Med* 2010; 51: 1624–1631. DOI: 10.2967/jnumed.110.078352.

20. Buchert R, Kluge A, Tossici-Bolt L, et al. Reduction in camera-specific variability in [(123)I]FP-CIT SPECT outcome measures by image reconstruction optimised for multisite settings: impact on age-dependence of the specific binding ratio in the ENC-DAT database of healthy controls. *Eur J Nucl Med Mol Imaging* 2016; 43: 1323–1336. DOI: 10.1007/s00259-016-3309-5.

21. Iida H, Narita Y, Kado H, et al. Effects of scatter and attenuation correction on quantitative assessment of regional cerebral blood flow with SPECT. *J Nucl Med* 1998; 39: 181–189.

22. Kim KM, Varrone A, Watabe H, et al. Contribution of scatter and attenuation compensation to SPECT images of nonuniformly distributed brain activities. *J Nucl Med* 2003; 44: 512–519.

23. Deloar HM, Watabe H, Kudomi N, et al. Dependency of energy and spatial distributions of photons on the object's edge in brain SPECT. *Ann Nucl Med* 2003; 17: 99–106. DOI: 10.1007/BF02988446.

24. Fujita M, Varrone A, Kim KM, et al. Effect of scatter correction on the compartmental measurement of striatal and extrastriatal dopamine D2 receptors using

[123I]epidepride SPET. *Eur J Nucl Med Mol Imaging* 2004; 31: 644–654. DOI: 10.1007/s00259-003-1431-7.

25. Yamauchi M, Imabayashi E, Matsuda H, et al. Quantitative assessment of rest and acetazolamide CBF using quantitative SPECT reconstruction and sequential administration of (123)I-iodoamphetamine: comparison among data acquired at three institutions. *Ann Nucl Med* 2014; 28: 836–850. DOI: 10.1007/s12149-014-0879-9.

26. Kim KM, Watabe H, Hayashi T, et al. Quantitative basal and vasareactive cerebral blood flow mapping using split-dose 123I-iodoamphetamine and single photon emission computed tomography. *NeuroImage* 2006; 33: 1126–1135. DOI: 10.1016/j.neuroimage.2006.06.064.

27. Shimochi S, Ihalainen J, Parikka V, et al. Small animal PET with spontaneous inhalation of (15)O-labelled oxygen gases: longitudinal assessment of cerebral oxygen metabolism in a rat model of neonatal hypoxic-ischaemic encephalopathy. *J Cereb Blood Flow Metab* 2023: 271678X231220691. DOI: 10.1177/0271678X231220691.

28. Mintun MA, Raichle ME, Martin WR, et al. Brain oxygen utilisation was measured with O-15 radiotracers and positron emission tomography. *J Nucl Med* 1984; 25: 177–187.

29. Iida H, Jones T and Miura S. Modeling approach to eliminate the need to separate arterial plasma in oxygen-15 inhalation positron emission tomography. *J Nucl Med* 1993; 34: 1333–1340.

30. Quarantelli M, Berkouk K, Prinster A, et al. Integrated software for analysing brain PET/SPECT studies with partial-volume-effect correction. *J Nucl Med* 2004; 45: 192–201.

31. Spetzler RF and Martin NA. A proposed grading system for arteriovenous malformations. *J Neurosurg* 1986; 65: 476–483. DOI: 10.3171/jns.1986.65.4.0476.

32. Iida H, Higano S, Tomura N, et al. Evaluation of regional differences of tracer appearance time in cerebral tissues using [15O] water and dynamic positron emission tomography. *J Cereb Blood Flow Metab* 1988; 8: 285–288. DOI: 10.1038/jcbfm.1988.60.

33. Iida H, Kanno I, Miura S, et al. A determination of the regional brain/blood partition coefficient of water using dynamic positron emission tomography. *J Cereb Blood Flow Metab* 1989; 9: 874–885. DOI: 10.1038/jcbfm.1989.121.

34. Ito H, Koyama M, Goto R, et al. Cerebral blood flow measurement with iodine-123-IMP SPECT, calibrated standard input function and venous blood sampling. *J Nucl Med* 1995; 36: 2339–2342.

35. Morgan MK, Winder M, Little NS, et al. Delayed haemorrhage following resection of an arteriovenous malformation in the brain. *J Neurosurg* 2003; 99: 967–971. DOI: 10.3171/jns.2003.99.6.0967.

36. Gowers WR. *A Manual of Disease of the Nervous System*. Volume 2. London: J & A Churchill, 1888: 341–351.

37. Spetzler RF, Wilson CB, Weinstein P, et al. Normal perfusion pressure breakthrough theory. *Clin Neurosurg* 1978; 25: 651–672. DOI: 10.1093/neurosurgery/25.cn_suppl_1.651.

38. Tyler JL, Leblanc R, Meyer E, et al. Hemodynamic and metabolic effects of cerebral arteriovenous malformations studied by positron emission tomography. *Stroke* 1989; 20: 890–898. DOI: 10.1161/01.str.20.7.890.

39. Homan RW, Devous MD, Sr., Stokely EM, et al. Quantification of intracerebral steal in patients with arteriovenous malformation. *Arch Neurol* 1986; 43: 779–785. DOI: 10.1001/archneur.1986.00520080027015.

40. Okabe T, Meyer JS, Okayasu H, et al. Xenon-enhanced CT CBF measurements in cerebral AVM's before and after excision. Contribution to pathogenesis and treatment. *J Neurosurg* 1983; 59: 21–31. DOI: 10.3171/jns.1983.59.1.0021.

41. Tarr RW, Johnson DW, Rutigliano M, et al. Use of acetazolamide-challenge xenon CT in assessing cerebral blood flow dynamics in patients with arteriovenous malformations. *AJNR Am J Neuroradiol* 1990; 11: 441–448.

42. Meyer B, Schaller C, Frenkel C, et al. Distributions of local oxygen saturation and its response to mean arterial blood pressure changes in the cerebral cortex adjacent to arteriovenous malformations. *Stroke* 1999; 30: 2623–2630. DOI: 10.1161/01.str.30.12.2623.

43. Hacein-Bey L, Nour R, Pile-Spellman J, et al. Adaptive changes of autoregulation in chronic cerebral hypotension with arteriovenous malformations: an acetazolamide-enhanced single-photon emission CT study. *AJNR Am J Neuroradiol* 1995; 16: 1865–1874.

44. Mast H, Mohr JP, Osipov A, et al. 'Steal' is an unestablished mechanism for the clinical presentation of cerebral arteriovenous malformations. *Stroke* 1995; 26: 1215–1220. DOI: 10.1161/01.str.26.7.1215.

45. Young WL, Pile-Spellman J, Prohovnik I, et al. Evidence for adaptive autoregulatory displacement in hypotensive cortical territories adjacent to arteriovenous malformations. Columbia University AVM Study Project. *Neurosurg* 1994; 34: 601–610; discussion 610–611. DOI: 10.1227/00006123-199404000-00006.

46. al-Rodhan NR, Sundt TM, Jr., Piepgras DG, et al. Occlusive hyperemia: a theory for the hemodynamic complications following resection of intracerebral arteriovenous malformations. *J Neurosurg* 1993; 78: 167–175. DOI: 10.3171/jns.1993.78.2.0167.

47. Iwama T, Hayashida K, Takahashi JC, et al. Cerebral hemodynamics and metabolism in patients with cerebral arteriovenous malformations: an evaluation using positron emission tomography scanning. *S* 2002; 97: 1314–1321. DOI: 10.3171/jns.2002.97.6.1314.

48. Fierstra J, Conklin J, Krings T, et al. Impaired peri-nidal cerebrovascular reserve in seizure patients with brain arteriovenous malformations. *Brain* 2011; 134: 100–109. DOI: 10.1093/brain/awq286.

49. Hashimoto N, Nozaki K, Takagi Y, et al. Surgery of cerebral arteriovenous malformations. *Neurosurg* 2007; 61: 375–387; discussion 387–379. DOI: 10.1227/01.NEU.0000255491.95944.EB.

50. Sato S, Kodama N, Sasaki T, et al. Perinidal dilated capillary networks in cerebral arteriovenous malformations. *Neurosurg* 2004; 54: 163–168; discussion 168–170. DOI: 10.1227/01.neu.0000097518.57741.be.

51. Sadato N, Yonekura Y, Senda M, et al. PET and the autoradiographic method with continuous inhalation of oxygen-15-gas: theoretical analysis and comparison with conventional steady-state methods. *J Nucl Med* 1993; 34: 1672–1680. 1993/10/01.

52. Lammertsma AA and Jones T. Low oxygen extraction fraction in tumours measured with the oxygen-15 steady state technique: effect of tissue heterogeneity. *Br J Radiol* 1992; 65: 697–700. DOI: 10.1259/0007-1285-65-776-697.

Figure Legends

Figure 1.

Four regions of interest (ROI) templates defining the remote regions for the ipsilateral (ROI-ri) and contralateral (ROI-rc) hemispheres (**A**) and the peri-nidal regions for the

ipsilateral (ROI-pi) and contralateral (ROI-pc) lateral hemispheres (**B)** are shown. Remote ROIs were placed in 10 anatomical regions on the magnetic resonance angiography (MRA) image on the ipsilateral side (ROI-ri) and mirror position (contralateral side) (ROI-rc). These ROIs were at least 20 mm from the nidus vessels; otherwise, they were excluded. The peri-nidus ROIs were placed on the MRA images in a position close to the nidus core to avoid overlapping the nidus vessel lesion. The ROIs placed on the MRA image were superimposed on the cerebral blood flow (***CBF***) image calculated using the dual-tracer basis function method (DBFM) in ^{15}O-positron emission tomography (PET), the ***CBF*** image calculated using dual-tracer autoradiography (DARG) in ^{15}O-PET, and the ***CBF*** calculated image using quantitative ^{123}I-IMP SPECT, which were aligned to the same slices on the MRA image. Note that a part of the brain disappeared in the ***CBF*** image calculated by DBFM and DARG (A). This happened during the process of masking the high concentration of radio gas (^{15}O-O_2) in the paranasal sinus during the initial process for parametric image calculation.

Figure 2.

A typical example of parametric images obtained from a representative case of right temporal AVM (case 2). **A: *CBF***, ***CMRO$_2$***, ***OEF*,** and the vascular activity contributions for ^{15}O-O_2 (***V_o***) and ^{15}O-H_2O (***V_w***) obtained by the DBFM calculation; **B: *CBF***, ***CMRO$_2$*,**

and ***OEF*** calculated by the DARG method with a ***CBV*** image calculated from ^{15}O-CO inhalation PET; **C**: quantitative ***CBF*** image obtained with quantitative ^{123}I-IMP SPECT, with MRA and DSA images. The DBFM method yielded ***CBF*** and $\boldsymbol{CMRO_2}$ images with reduced values in the nidal region, while ***CBF*** and $\boldsymbol{CMRO_2}$ calculated by the DARG method resulted in large increases in the nidal region. Increased $\boldsymbol{V_o}$ and $\boldsymbol{V_w}$ were seen in the nidal region, which is similar to those in the ***CBV*** images, but there were significant differences between $\boldsymbol{V_o}$ and $\boldsymbol{V_w}$. In this article, we defined $\boldsymbol{V_o}$ as corresponding to the radioactivity in the arteriole and non-extracted ^{15}O-O_2 in the form of ^{15}O-O_2-labelled oxy-haemoglobin in the venule. We also assumed that $\boldsymbol{V_w}$ corresponds to the radioactivity in the form of ^{15}O-H_2O in the arteriole, where the venule radioactivity is increased due to the shunt vessels. Normally, $\boldsymbol{V_w}$ is not seen in healthy individuals or patients with ischaemic diseases because ^{15}O-H_2O reaches equilibrium to tissue; thus, the radioactivity in the venule is equal to that in the tissue. Elevated $\boldsymbol{V_w}$ in this study is attributed to the arteriovenous shunt causing a fraction of the arterial blood to be carried to the sinus vein resulting in the radioactivity from ^{15}O-H_2O becoming visible in the venule. Note that at the top of the ***OEF*** images calculated by both DBFM and DARG, there is an area with high ***OEF***, which is thought to be because of either the radio gases in the trachea duct or external gas that leaked out of the mask during the PET measurement. While this activity is not seen often, it is seen in many cases.

Abbreviations: CBF, cerebral blood flow; $CMRO_2$, cerebral oxygen metabolism rate; OEF, oxygen extraction fraction; CBV, cerebral blood volume; DBFM, dual-tracer basis function method; DARG, dual-tracer autoradiography; ^{123}I-IMP SPECT, ^{123}I-iodoamphetamine single-photon emission computed tomography; ROI, region of interest; DSA, digital subtraction angiography; MRA, magnetic resonance angiography

Figure 3.

Typical time-activity curves were observed in a patient with AVM in this study. **A:** Arterial input function for the total blood (black solid line), ^{15}O-O_2 (blue solid line), and ^{15}O-H_2O (green solid line). (**B**) Regional tissue time-activity curves in a patient with AVM (case 2) were obtained from a contralateral region (ROI-pc). Black circles correspond to the measured time-activity curve. The black solid line represents the fit result for the total blood curve, while the blue and green lines correspond to the responses to the ^{15}O-O_2 AIF and the ^{15}O-H_2O calculated as the 1st and 2nd terms of Eq. (1), respectively. The solid red curve represents the vascular components, including the $\boldsymbol{V_o}$ and $\boldsymbol{V_w}$ contributions, as presented as the third and fourth terms in Eq. (1). **C**, **D**, and **E** similarly represent the time-activity curves with the same notations in the peri-nidus, transitional, and intra-nidal regions, respectively. The tissue time-activity curves were well reproduced in all cases with the formulation in Eq. 1, suggesting the adequacy of the model assumed in this study.

Abbreviations: AVM, arteriovenous malformation; AIF, arterial input function; ROI, region of interest

Figure 4.

Summary results from Pearson's regression analysis demonstrate the correlations in ***CBF*** (**A**), ***CMRO₂*** (**B**), and ***OEF*** (**C**) between the DBFM and DARG methods for four criteria of ROIs in the remote ipsilateral (ROI-ri), remote contralateral (ROI-rc), peri-nidus ipsilateral (ROI-pi), and peri-nidus contralateral (ROI-pc) regions.

Higher correlations were observed in all the remote (both ROI-ri and ROI-rc) and peri-nidus contralateral (ROI-pc) regions than in the peri-nidus ipsilateral (ROI-pi) regions (r = 0.79 in ***CBF***, 0.60 in ***CMRO₂*** and 0.80 in ***OEF***). DARG tended to overestimate CBF and ***CMRO₂*** in ROI-pi. In the ***OEF*** comparison, overestimation occurs in the DARG calculation in areas with a smaller ***OEF***.

Abbreviations: CBF, cerebral blood flow; $CMRO_2$, cerebral oxygen metabolism rate; OEF, oxygen extraction fraction; DBFM, dual-tracer basis function method; DARG, dual-tracer autoradiography; ROI, region of interest

Figure 5.

Relationships of ***CBF*** values between DBFM and ^{123}I-IMP SPECT and between DARG and ^{123}I-IMP SPECT in the peri-nidus ipsilateral (ROI-pi) and peri-nidus contralateral (ROI-pc) regions. In DBFM, a significant positive correlation was observed in ***CBF*** values in both the contralateral ROI-pc and ipsilateral ROI-pi. In DARG, a significant positive correlation was also observed in ***CBF*** values between ^{123}I-IMP SPECT and DARG in the contralateral ROI-pc. Nonetheless, the correlation was lower on the ipsilateral ROI-pi (r = 0.39, p = 0.001). The Brand-Altman correlation plots for ***CBF*** values revealed a proportional difference variability between DBFM and ^{123}I-IMP SPECT measurements as well as DARG and ^{123}I-IMP SPECT measurements. A relatively wide range of lower and upper limits of agreement (reference value) was observed in the ipsilateral ROI-pi between DARG and ^{123}I-IMP SPECT.

Abbreviations: CBF, cerebral blood flow; DBFM, dual-tracer basis function method; DARG, dual-tracer autoradiography; ^{123}I-IMP SPECT, ^{123}I-iodoamphetamine single-photon emission computed tomography; ROI, region of interest

Figure 6.

Relationships of ***CBF*** values between DBFM, DARG, and ^{123}I-IMP SPECT measurements in the ipsilateral peri-nidus (ROI-pi), ipsilateral intra-nidus (ROI-n), and ipsilateral transitional border of nidus (ROI-t) regions. Note that for values higher than

the dashed line in the figure, the axis scale is different from that below this line. A large dissociation occurred between DBFM and DARG (A), as well as between DARG and ^{123}I-IMP SPECT (B). On the other hand, the correlation between DBFM and ^{123}I-IMP SPECT was maintained (C).

Abbreviations: CBF, cerebral blood flow; DBFM, dual-tracer basis function method; DARG, dual-tracer autoradiography; ^{123}I-IMP SPECT, ^{123}I-iodoamphetamine single-photon emission computed tomography; ROI, region of interest

Tables

Table 1. The baseline characteristics of patients with unruptured cerebral arteriovenous malformations.

Case	Age	Sex	Presentation	Location of nidus	Side	Size of nidus (mm)	Eloquence of adjacent brain	Deep venous drainage	S-M grade	The following treatment
1	26	Female	Asymptomatic	Frontal	R	34	No	Yes	3	Surgical resection
2	30	Female	Asymptomatic	Temporal	R	30	No	Yes	3	Gamma knife
3	23	Female	Asymptomatic	Thalamus	L	38	Yes	Yes	4	Gamma knife
4	43	Male	Dysarthria	Thalamus	L	43	Yes	Yes	4	Gamma knife
5	59	Male	Chemosis	Mesial temporal	R	37	No	Yes	3	Gamma knife
6	23	Female	Seizure	Frontal	R	45	Yes	No	3	Gamma knife
7	36	Female	Seizure	Frontal	L	70	Yes	Yes	5	Observation

Abbreviations: R, right; L, left; S-M grade, Spetzler–Martin grade

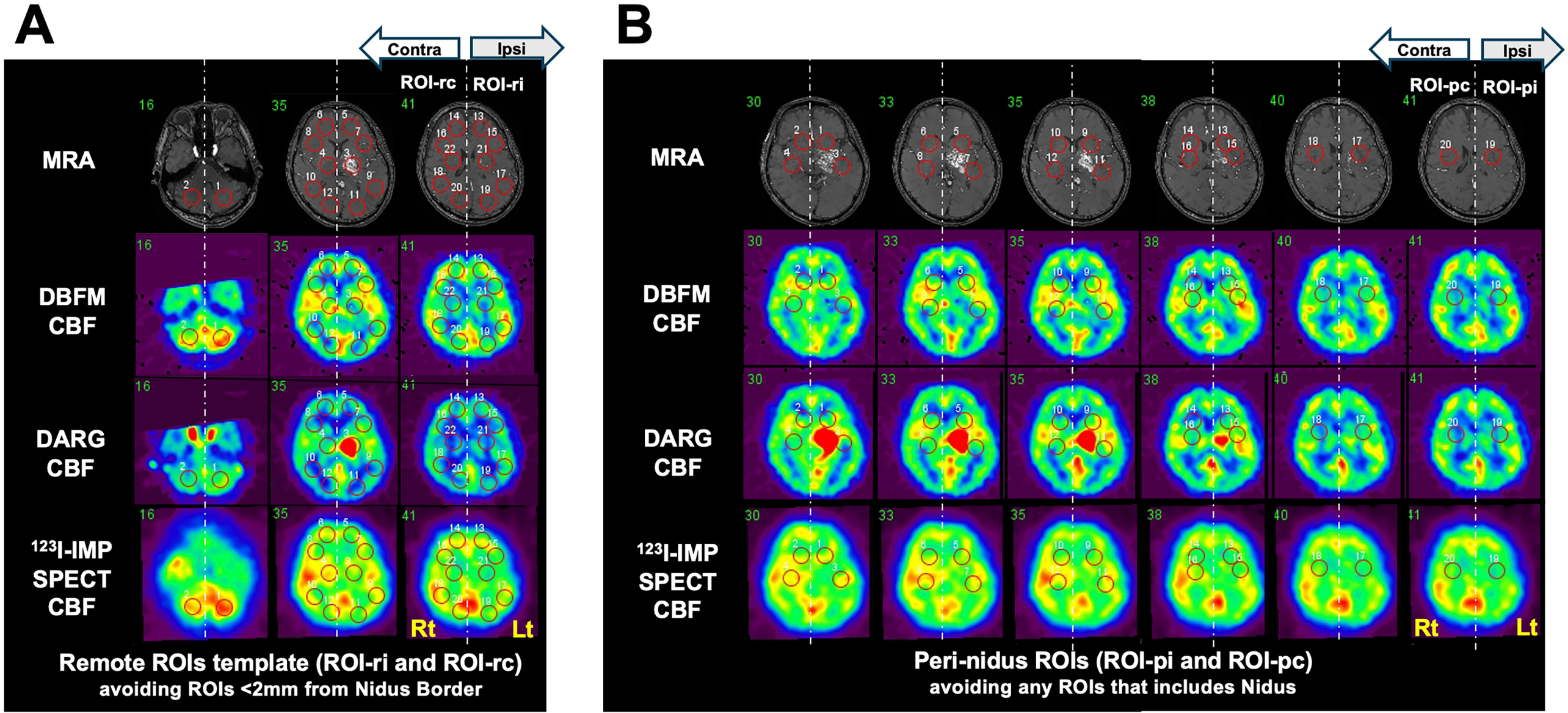
A
Contra
Ipsi
ROI-rc
ROI-ri
MRA
DBFM CBF
DARG CBF
123I-IMP SPECT CBF
Rt
Lt
Remote ROIs template (ROI-ri and ROI-rc)
avoiding ROIs <2mm from Nidus Border
B
Contra
Ipsi
ROI-pc
ROI-pi
MRA
DBFM CBF
DARG CBF
123I-IMP SPECT CBF
Rt
Lt
Peri-nidus ROIs (ROI-pi and ROI-pc)
avoiding any ROIs that includes Nidus

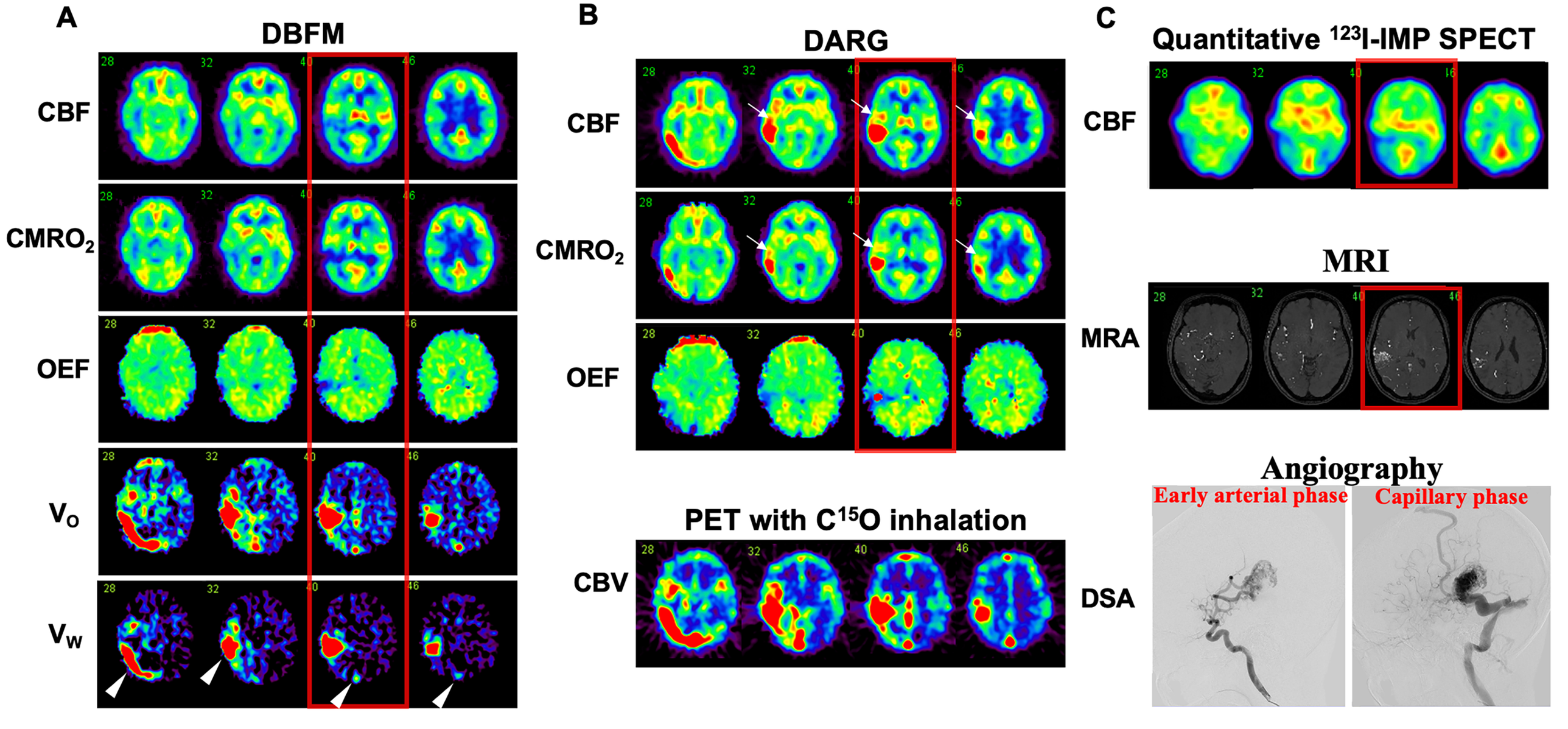
A
DBFM
CBF
CMRO2
OEF
VO
VW
B
DARG
CBF
CMRO2
OEF
PET with C15O inhalation
CBV
C
Quantitative 123I-IMP SPECT
CBF
MRI
MRA
Angiography
Early arterial phase
Capillary phase
DSA

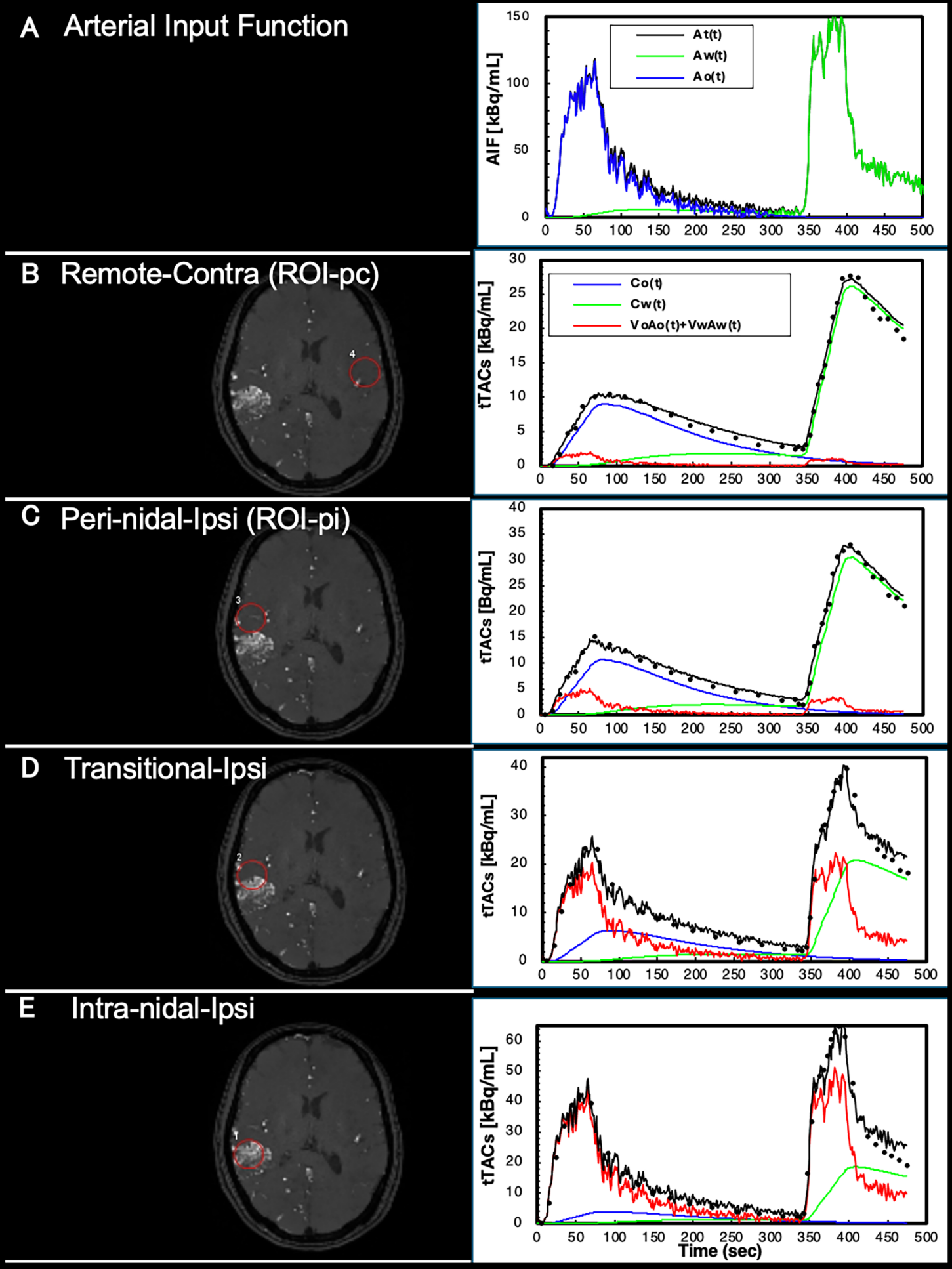
A Arterial Input Function
AIF [kBq/mL]
At(t)
Aw(t)
Ao(t)
B Remote-Contra (ROI-pc)
4
tTACs [kBq/mL]
Co(t)
Cw(t)
VoAo(t)+VwAw(t)
C Peri-nidal-Ipsi (ROI-pi)
3
tTACs [Bq/mL]
D Transitional-Ipsi
2
tTACs [kBq/mL]
E Intra-nidal-Ipsi
1
tTACs [kBq/mL]
Time (sec)

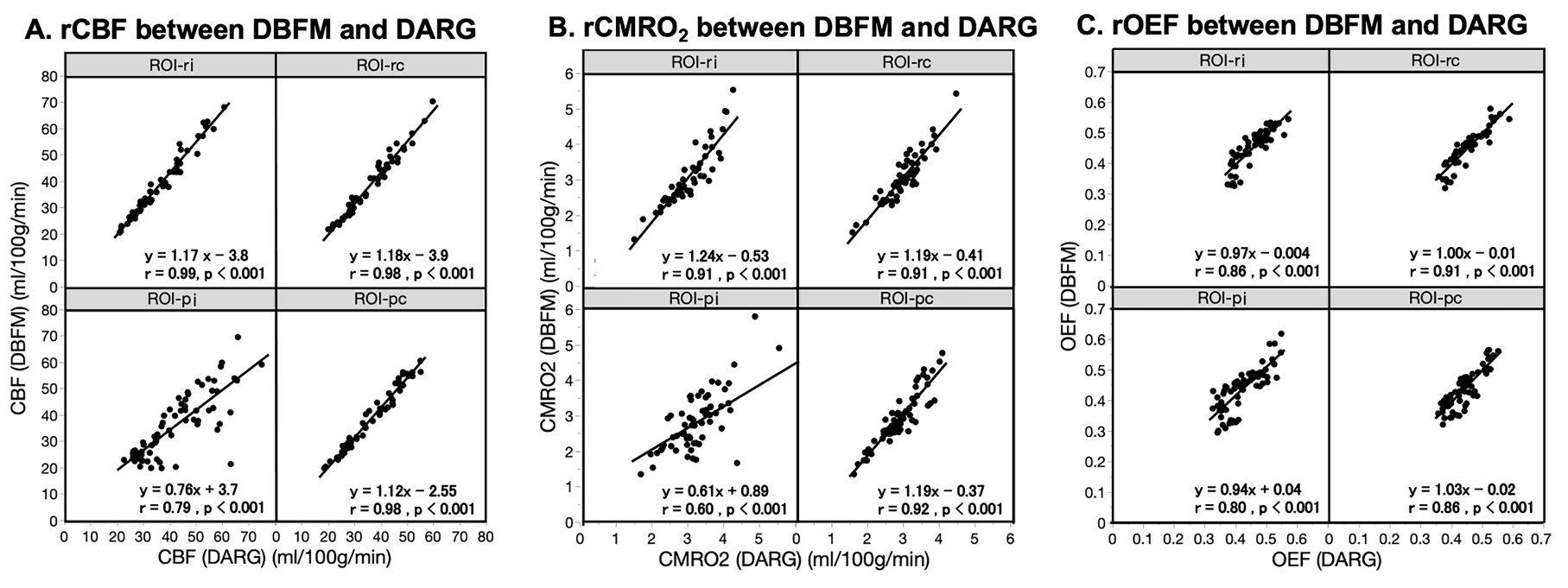
A. rCBF between DBFM and DARG
ROI-ri
ROI-rc
ROI-pi
ROI-pc
y = 1.17 x − 3.8
r = 0.99, p < 0.001
y = 1.18x − 3.9
r = 0.98 , p < 0.001
y = 0.76x + 3.7
r = 0.79 , p < 0.001
y = 1.12x − 2.55
r = 0.98 , p < 0.001
CBF (DBFM) (ml/100g/min)
CBF (DARG) (ml/100g/min)
B. rCMRO2 between DBFM and DARG
y = 1.24x − 0.53
r = 0.91 , p < 0.001
y = 1.19x − 0.41
r = 0.91 , p < 0.001
y = 0.61x + 0.89
r = 0.60 , p < 0.001
y = 1.19x − 0.37
r = 0.92 , p < 0.001
CMRO2 (DBFM) (ml/100g/min)
CMRO2 (DARG) (ml/100g/min)
C. rOEF between DBFM and DARG
y = 0.97x − 0.004
r = 0.86 , p < 0.001
y = 1.00x − 0.01
r = 0.91 , p < 0.001
y = 0.94x + 0.04
r = 0.80 , p < 0.001
y = 1.03x − 0.02
r = 0.86 , p < 0.001
OEF (DBFM)
OEF (DARG)

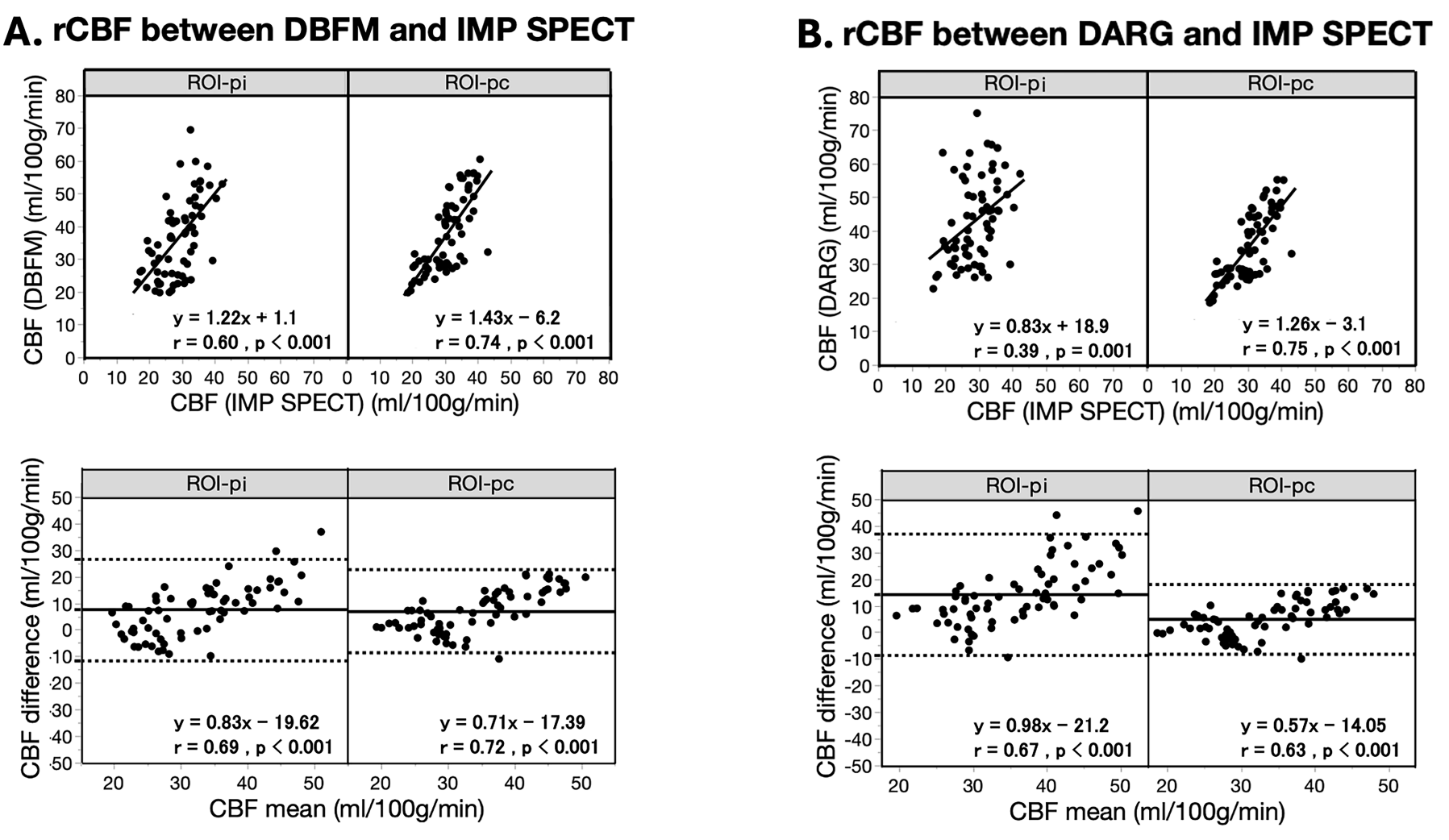
A. rCBF between DBFM and IMP SPECT
ROI-pi
ROI-pc
CBF (DBFM) (ml/100g/min)
y = 1.22x + 1.1
r = 0.60 , p < 0.001
y = 1.43x − 6.2
r = 0.74 , p < 0.001
CBF (IMP SPECT) (ml/100g/min)
CBF difference (ml/100g/min)
y = 0.83x − 19.62
r = 0.69 , p < 0.001
y = 0.71x − 17.39
r = 0.72 , p < 0.001
CBF mean (ml/100g/min)
B. rCBF between DARG and IMP SPECT
CBF (DARG) (ml/100g/min)
y = 0.83x + 18.9
r = 0.39 , p = 0.001
y = 1.26x − 3.1
r = 0.75 , p < 0.001
y = 0.98x − 21.2
r = 0.67 , p < 0.001
y = 0.57x − 14.05
r = 0.63 , p < 0.001

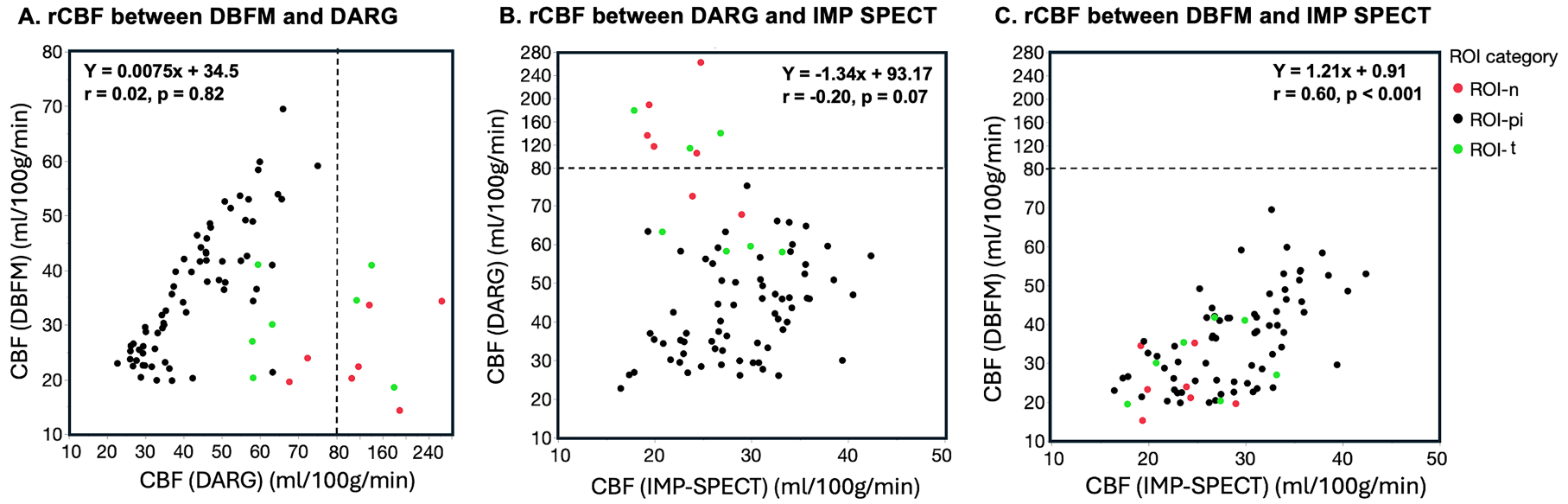
A. rCBF between DBFM and DARG
Y = 0.0075x + 34.5
r = 0.02, p = 0.82
CBF (DBFM) (ml/100g/min)
CBF (DARG) (ml/100g/min)
B. rCBF between DARG and IMP SPECT
Y = -1.34x + 93.17
r = -0.20, p = 0.07
CBF (DARG) (ml/100g/min)
CBF (IMP-SPECT) (ml/100g/min)
C. rCBF between DBFM and IMP SPECT
Y = 1.21x + 0.91
r = 0.60, p < 0.001
CBF (DBFM) (ml/100g/min)
CBF (IMP-SPECT) (ml/100g/min)
ROI category
ROI-n
ROI-pi
ROI-t